Korean J. Chem. Eng., 38(9), 1834-1842 (2021)
DOI: 10.1007/s11814-021-0871-8

pISSN: 0256-1115
eISSN: 1975-7220

Characteristics of $Sr_{0.92}Y_{0.08}Ti_{1-x}Ni_xO_{3-\delta}$ anode for direct internal steam methane reforming in solid oxide fuel cells

Jun Ho Kim, Su In Mo, Gwang Seon Park, and Jeong Woo Yun[†]

School of Chemical Engineering, Chonnam National University, Gwangju 61186, Korea

(*Received 10 March 2021 • Revised 14 May 2021 • Accepted 19 June 2021*)

Abstract−$Sr_{0.92}Y_{0.08}Ti_{1-x}Ni_xO_{3-\delta}$ (SYTN) having a perovskite structure was investigated as a direct internal steam methane reforming catalyst for use in solid oxide fuel cells. To analyze the effect of Ni-ion doping, 0, 3, and 5 mol% of Ni is doped at the B-site of $Sr_{0.92}Y_{0.08}TiO_{3-\delta}$ (SYT). On doping, each Ni^{2+} cation substitutes a Ti^{4+} cation in SYT to form an oxygen vacancy with two electron holes, thus acting as an oxygen-ion conductor. The number of oxygen vacancies increases with increase in Ni-ion doping. In particular, $Sr_{0.92}Y_{0.08}Ti_{0.95}Ni_{0.05}O_{3-\delta}$ (SYTN5) shows excellent catalytic activity for steam methane reforming, yielding CH_4 conversions of 0.80, 0.96, and 0.99 at 700, 800, and 900 °C, respectively, and H_2-to-CO ratios of 3.38, 3.32 and 3.24 at 700, 800, and 900 °C, respectively, which are very close to the theoretical values for the steam methane reforming and water gas shift reactions. The excellent electrochemical property and high oxygen-ion conductivity of the SYTN5 anode result in good cell performance.

Keywords: Solid Oxide Fuel Cells, Steam Methane Reforming, Ni-ion Doping, Alternative Anode, Carbon Deposition

INTRODUCTION

Solid oxide fuel cells (SOFCs) have received much attention because of their high energy-conversion efficiency and fuel source flexibility. In particular, high-temperature SOFC operation allows the internal reforming of various commercial fuel sources, including natural gas, gasoline, and diesel [1,2], and the direct use of these hydrocarbon fuels provides several physiochemical advantages over the use of pure H_2, including easy storage/transport and high energy density. In addition, internal reforming eliminates the need for external reforming and fuel purification processes, thus improving the overall system efficiency and reducing the operating cost of SOFCs.

Methane, a major component in natural gas and shale gas, is an attractive energy source because it is cheap and abundant. CH_4 can be utilized by direct internal reforming using H_2O or CO_2 in SOFCs. Although CO_2 reforming (dry methane reforming, DMR) has attracted attention recently, especially in bio-gas utilization, steam methane reforming (SMR) remains the most common method for H_2 production and direct internal reforming in SOFCs [3-6]. In the SOFC, CH_4 reacts with H_2O to produce H_2 and CO via SMR, as shown in reaction (1), and the produced CO reacts with H_2O to produce CO_2 and H_2 via the water-gas shift (WGS) reaction, as shown in reaction (2).

$$CH_4+H_2O \rightarrow CO+3H_2 \qquad \Delta_r H^o=206\ \text{kJ/mol} \tag{1}$$

$$CO+H_2O \rightarrow CO_2+H_2 \qquad \Delta_r H^o=-41.2\ \text{kJ/mol} \tag{2}$$

Because the WGS reaction is much faster than the SMR reaction, it can be assumed to be at or near equilibrium [7,8].

Although SMR has been successfully utilized in industrial technology, its application to SOFCs is challenging, both in terms of reactor design and catalyst performance. In particular, the difference in the reaction rates between the SMR reaction and electrochemical oxidation reaction could be a major problem for direct internal reforming in the SOFC anode. Specifically, H_2 and oxygen ions (O^{2-}) can react electrochemically at the anode to produce current, steam, and heat, as shown in reaction (3).

$$H_2+O^{2-} \rightarrow H_2O+2e \tag{3}$$

The interactions between the slow, endothermic SMR reaction and the fast, exothermic H_2 electrochemical oxidation reaction are very complicated and not well understood.

Currently, Ni/yttria-stabilized zirconia (YSZ) is widely used as an SOFC anode, but it has critical limitations, for example, suffering from coking, sintering, and poisoning during the utilization of hydrocarbon fuels including CH_4. In addition, during the direct internal SMR in SOFCs, carbon deposition can be major problem under H_2O-limited conditions. Specifically, because of the high catalytic activity of Ni catalysts for C-H bond breaking, carbon is undesirably formed on the Ni phase, and this carbon deposit blocks the porous anode and increases the diffusion resistance for the fuel gas. Moreover, carbon deposition and precipitation leads to volume expansion in the anode and, thus, the separation of the Ni and YSZ phases. This results in internal stress and the structural rupture of the anode. To minimize carbon deposition during SMR, the use of a high H_2O/CH_4 ratio in the feed, in which H_2O acts as an oxidant, is recommended [9]. A high H_2O/CH_4 ratio, however, dilutes the fuel, resulting in lower electrochemical efficiency and H_2 yield, as well as higher operating cost as a result of the need for H_2O evaporation. Therefore, the development of alternative anode materials that are resistant to coking and poisoning is required to utilize commercial hydrocarbon fuels including CH_4. These alternative anodes

---

[†] To whom correspondence should be addressed.

E-mail: jwyun@jnu.ac.kr

should meet strict requirements for use in SOFCs [10-12]: specifically, the anode materials should have (i) good electrocatalytic activity for hydrocarbon fuel oxidation, (ii) chemical stability at high temperature, (iii) chemical compatibility with the electrolyte, (iv) high resistivity against carbon coking and impurity poisoning, for example, by sulfur compounds, and (v) sufficient ionic and electronic conductivity. Based on these criteria, many researchers have developed alternative SOFC anodes for the direct and practical utilization of hydrocarbon fuels. Although Ni can be replaced by metals such as Cu, W, Co, Pd, and Ru to yield well-performing alternative anode materials, they are not appropriate for use with hydrocarbon fuels, especially for long-term operation [13-18]. In particular, noble metals such as Pt, Ru, and Pd are prohibitively expensive. In contrast, oxide-based materials are good candidates for SOFC anode materials. Due to their low electrical and chemical activity for methane oxidation, most oxides are intrinsically immune to carbon deposition problems [19,20]. In particular, perovskites having an ABO_3 stoichiometry can be modified by the substitution of rare-earth cations or lanthanide cations at the A-site, and transition metal cations can substitute the B-site cations. In A-site-doped perovskites, the A-site cations have multiple valence states depending on the oxygen partial pressure; this results in the delocalization of electrons and improved electronic conductivity. Further, the doping of cations having unmatching valences into the B-site could result in the production of oxygen vacancies, thus improving the ionic conductivity. This mixed ionic-electronic conducting (MIEC) property exhibited by some doped perovskites is a significant advantage in alternative anodes because electrochemical oxidation is not only confined to the triple phase boundary but also occurs at the gas-solid two-phase boundary (2PB). Therefore, various doped perovskites have been studied as alternative anodes for the utilization of hydrocarbon fuels [21-25]. In our previous studies, the electrochemical properties of $Sr_2Ni_{1.8}Mo_{0.2}O_{6-\delta}$ (SNMO) [26,27] $Sr_{0.92}Y_{0.08}Ti_{1-x}Fe_xO_{3-\delta}$ (SYTF) [28,29], $Sr_{0.92}Y_{0.08}Ti_{1-x}Ni_xO_{3-\delta}$ (SYTN) [30], and $Sr_{0.92}Y_{0.08}Ti_{1-x}Ru_xO_{3-\delta}$ (SYTRu) [31] were investigated in the presence of H_2 and CH_4 fuels.

In this study, we investigated the catalytic property of SYTN materials as SMR catalysts. To prepare SYTN, $Sr_{0.92}Y_{0.08}TiO_{3-\delta}$ (SYT) was doped with various amounts of Ni (0-5 mol%) to investigate the effects of Ni-ion doping on the SMR behavior. We found that the MIEC property exhibited by SYTN enhances the electrocatalytic performance of the anode and results in improved cell performance.

EXPERIMENTAL

To synthesize SYTN, strontium nitrate ($Sr(NO_3)_2$, Aldrich), yttrium nitrate hexahydrate ($Y(NO_3)_2 \cdot 6H_2O$, Aldrich), nickel nitrate ($Ni(NO_3)_2$, Aldrich), and titanium isopropoxide ($Ti[OCH(CH_3)_2]_4$, Junsei) were prepared with some additives. To investigate the effect of the doping of the $Sr_{0.92}Y_{0.08}TiO_{3-\delta}$ (SYT) anode with Ni on the SMR performance, the amount of Ni was varied, i.e., 0, 3, and 5 mol%. The procedure for the synthesis of SYTN has been described in our previous work [30]. The crystal structure of SYTN was analyzed using X-ray diffractometry (XRD, Rigaku, RINT-5200) with Cu K_α radiation (λ=1.5405 nm) generated at 30 kV and 30 mA. Temperature-programmed reduction (TPR) experiments on the fresh catalyst were carried out in a BEL TPR device (BEL CAT, BEL Japan, Inc). The flow rate of the reactive gas (4% H_2/Ar) over the catalyst (50 mg) was 50 sccm, and the reaction temperature was increased in increments of 5 °C min^{-1} from 100 to 900 °C. The surface area and pore diameter distribution of the catalysts were obtained using an adsorption analyzer (Micromeritics ASAP 2020 apparatus) and the Brunauer-Emmett-Teller (BET) method.

The SMR reaction with the SYTN catalyst was carried out at atmospheric pressure in a fixed-bed continuous flow system. A quartz tube having an internal diameter of 2 mm was used as the reactor, and 0.4 g of SYTN catalyst was loaded onto quartz wool and placed in the reactor. The catalysts were reduced in 10% H_2/Ar flow in situ at 900 °C for 2 h before the SMR reaction was carried out. A mixed gas (CH_4/H_2O=10/10 sccm) was used for SMR at a gas hourly space velocity (GHSV) of 6,000 h^{-1}. The products of the reaction were analyzed using gas chromatography (GC, Agilent 6900 model), and the GC device was connected to a thermal conductivity detector (TCD).

To investigate the electrochemical performance of SYTN as an anode material, electrolyte supported cells were fabricated having a thickness of 0.8 mm and a diameter of 25.4 mm. The electrolyte supports were prepared by uniaxial dry pressing (Carver Press Inc., USA) using 8 mol% Y_2O_3/ZrO_2 powder (8YSZ, $Zr_{0.92}Y_{0.08}O_{2-\delta}$, Fuel Cell Materials, USA), followed by sintering at 1,400 °C for 5 h. The prepared SYTN slurry with a polymethylmethacrylate (PMMA) pore former, binder, and other additives was coated on the dense 8YSZ electrolyte support by tape casting to yield the anode. The anodes had an active area of 0.79 cm^2 and thickness of approximately 30-50 μm after cofiring with the electrolyte support at 1,200 °C for 5 h. An $La_{0.85}Sr_{0.15}MnO_3$ (LSM) paste was coated on the 8YSZ electrolyte using the tape casting method and then fired at 1,100 °C to prepare the cathode. The anode microstructure was analyzed using field-emission scanning electron microscopy (FE-SEM, Hitachi, S-4200, Japan). The electrochemical performance was investigated by mounting an electrolyte-supported button cell between double-layered alumina tubes and sealing it with Pyrex glass on the dense electrolyte. A perforated Pt plate (1 cm^2 in area) and Ag paste were used as current collectors. The electrochemical characteristics of the anodes were measured using electrochemical impedance spectroscopy (SP-150, Biologic Science Instrument). The impedance spectra were recorded in the frequency range of 10^{-2} to 10^6 Hz at an excitation voltage of 10 mV to ensure a linear response. The impedance analyses were performed when the Nyquist plot indicated an equilibrium state. For the anode, humidified hydrogen (approximately 8 vol% H_2O) and humidified CH_4 (approximately 8 vol% H_2O) were used as the fuel gases and were supplied at a rate of 200 mL·min^{-1}. For the cathode, air as an oxidant gas was supplied at a rate of 200 mL·min^{-1}.

RESULTS AND DISCUSSION

Fig. 1(a) shows the XRD patterns of the SYTN powder sintered at 1,200 °C. The amount of Ni as a B-site dopant was 3 or 5 mol% (SYTN3 and SYTN5, respectively), but the unmodified powder (SYTN0) was also tested. The ex situ XRD data were obtained after

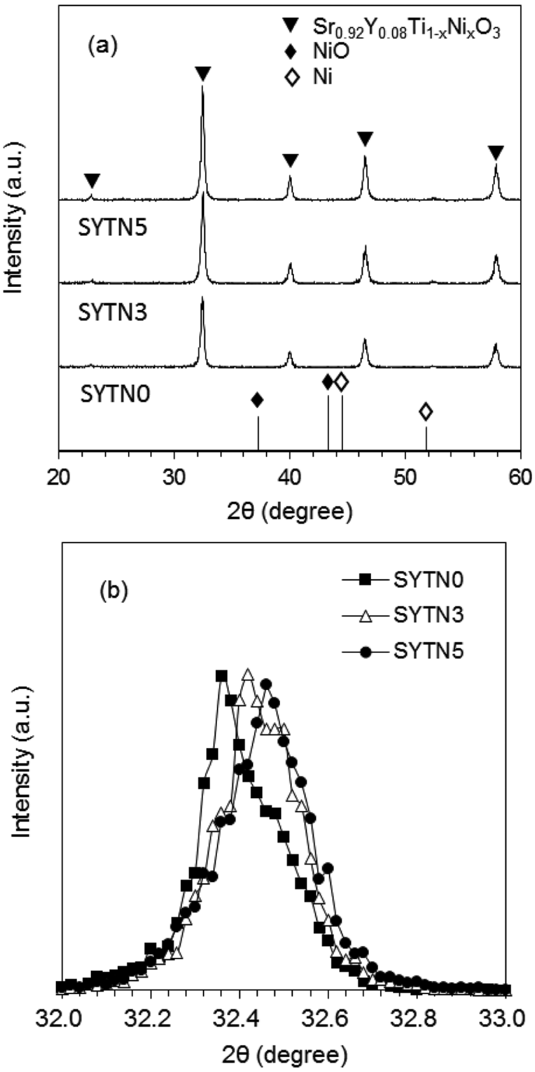

Fig. 1. (a) XRD patterns of SYTN0, SYTN3, and SYTN5 and (b) peak shift change with increase in Ni-ion doping.

perovskite structure formation at 600 °C for 10 h. No noticeable peaks other than those of $SrTiO_3$ having a perovskite structure were detected in the XRD patterns of all samples. However, all peaks shifted slightly to the right with increase in the amount of the Ni dopant, as shown in Fig. 1(b). In our previous research, SrO and NiO phases were detected in 7 mol% Ni-doped SYT (SYTN7) powder and were found to be segregated at the SYTN surface [30]. The larger ionic radius of Ni^{2+} (0.69 Å) compared to that of Ti^{4+} (0.61 Å) limits the amount of Ni^{2+} dopant at the six-coordinate B-site. As a result of the substitution of cations having different ionic radii into the crystal structure, the crystal strain changes, and this is described by the tolerance factor of the SYTN perovskite. The tolerance factor in doped perovskite is given by Eq. (4).

$$\tau=\frac{(1-x)\cdot R_A+x\cdot R_{A'}+R_O}{\sqrt{2}((1-y)\cdot R_B+y\cdot R_{B'}+R_O)} \qquad (4)$$

Here, x and y are the mole fractions of dopants at the A- and B-sites, respectively, R_A is the ionic radius of the A cation, $R_{A'}$ is the ionic radius of the A-site dopant, R_B is the ionic radius of the B cation, $R_{B'}$ is the ionic radius of the B-site dopant, and R_O is the ionic radius of the oxygen anion. The tolerance factor for SYTN0 is 0.9945 and it decreased with increase in Ni-ion doping at the B-site for SYTN3 and SYTN5, i.e., 0.9932 and 0.9924, respectively. The tolerance value of $SrTiO_3$ having an ideal perovskite structure is 1. The ionic radius of Y^{3+} (1.19 Å) is smaller than that of Sr^{2+} (1.44 Å) for A-site doping and the larger ionic radius of Ni^{2+} (0.69 Å) than that of Ti^{4+} (0.605 Å) reduced the tolerance value to less than 1; it decreased further with increase in Ni-ion doping. The decreasing tolerance value is a result of the tilting of the BO_6 octahedra to fill the increased space caused by the doping, and the symmetry of the crystal structure is, thus, lowered. This is the cause of the slight peak shift observed in the X-ray patterns of SYTN3 and the SYTN5. Perovskite is stable at tolerance factors of 0.75-1, and the cubic perovskite structure was still observed in the XRD patterns of SYTN0, SYTN3, and SYTN5, which have tolerance factors of 1±0.05.

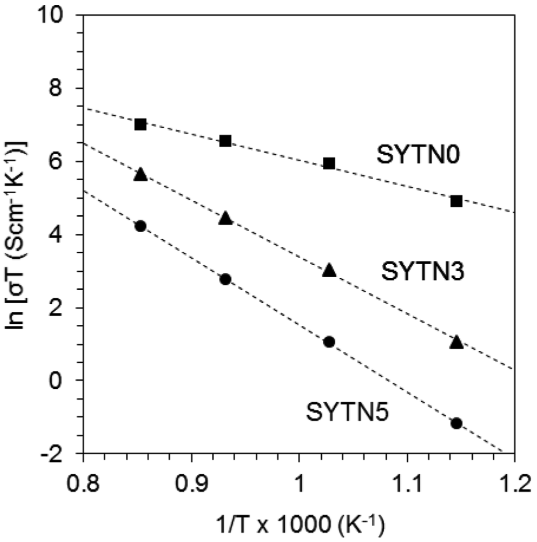

Fig. 2. Arrhenius plots of the electrical conductivity of SYTN0, SYTN3, and SYTN5 in 5% H_2 balanced with N_2 from 600 to 900 °C.

Fig. 2 shows Arrhenius plots of the electrical conductivities of the SYTN0, SYTN3, and SYTN5 samples in 5% H_2 balanced with N_2 at temperatures from 600 to 900 °C. The electrical conductivity data were obtained using a four-point probe direct current (DC) method. The electrical conductivity increased with increase in temperature, which is typical temperature-dependent behavior of ceramic materials. However, the electrical conductivity decreased with increase in Ni-ion doping. At 900 °C, the electrical conductivities were 0.95, 0.24, and 0.06 $S\cdot cm^{-1}$ for SYTN0, SYTN3, and STYN5, respectively. The straight dashed lines shown in Fig. 2 are linear least-square fits of the electrical conductivities, and the activation energies obtained from the linear fits (determined using Eq. (5)) are summarized in Table 1.

$$\sigma\cdot T=\sigma_0\cdot\exp\left(\frac{E_A}{k_BT}\right) \qquad (5)$$

Here, σ_0 is a pre-exponential factor related to the effective num-

Table 1. Activation energy and pre-exponential factor under H_2 fuel conditions obtained using the data shown in Fig. 2

	E_σ (eV)	A_σ ($S\cdot cm^{-1}\cdot K^{-1}$)	R^2 (-)
SYTN0	0.616	5.33×10^{5}	0.989
SYTN3	1.338	1.62×10^{8}	0.999
SYTN5	1.585	4.48×10^{8}	0.999

ber of formed electrons and mobile oxygen ions, E_A is the activation energy for electrical conduction, and k_B and T denote the Boltzmann constant and absolute temperature, respectively. The activation energy of the SYTN samples increased with increase in Ni-ion doping. The decrease in the electrical conductivity could be a result of aliovalent substitution at both the A- and B-sites of $SrTiO_3$. At the A-site, Y^{3+} cations having an ionic radius of 1.19 Å in a twelve-coordinate site could substitute the Sr^{2+} cations (1.44 Å in the same environment). This aliovalent cation substitution results in the formation of lattice defects to maintain the electrical neutrality of the crystals, leading to n-type semi-conductive behavior. Ti^{4+} (ionic radius of 0.69 Å in a six-coordinate site) in the B-site of $SrTiO_3$ could be substituted by Ni^{2+} (ionic radius of 0.605 Å in a six-coordinate site) resulting in the creation of oxygen vacancies with a pair of electron holes. The mechanism of aliovalent substitution at the A- and B-sites of $SrTiO_3$ can be described by Eqs. (6) and (7).

$$Y_2O_3 \xrightarrow{SrO} 2Y^{o}_{Sr} + 3O^{X}_{O} + V_{Sr} + 2e \tag{6}$$

$$NiO \xrightarrow{TiO_2} Ni''_{Ti} + O^{X}_{O} + V^{oo}_{O} \tag{7}$$

In the A-site mechanism (Eq. (6)), two Sr^{2+} ions in the $SrTiO_3$ lattice are substituted by Y^{3+} from Y_2O_3, which results in the formation of strontium vacancies and two electrons to maintain the electrical neutrality of the crystals. The Y^{3+} substitution results in n-type semi-conductive behavior. In the B-site mechanism (Eq. (7)), Ni^{2+} can substitute Ti^{4+} at the B-site of $SrTiO_3$ to form an oxygen vacancy with electron holes. These oxygen vacancies contribute to the ionic conductivity of SYTN. In addition, the TiO_2 in $SrTiO_3$ can be reduced to $TiO_{2-\delta}$ under reducing conditions, leading to the formation of additional oxygen vacancies and the improvement in ionic conductivity. In this study, however, the electrical conductivity reduced with increase in the amount of Ni^{2+} dopant. The MIEC property could be the origin of the decrease in electrical conductivity with increase in Ni-ion doping. The electron pairs formed via Eq. (6) and oxygen vacancies with electron holes formed via Eq. (7) could become associated at high temperatures. Therefore, the electronic conductivity might be reduced via the defect association of oxygen vacancies with electron holes after B-site modification. Because the electronic conductivity of MIEC materials is much larger than the ionic conductivity, it makes the largest contribution to the overall conductivity. Therefore, the electronic conductivity arising from defect association in the SYTN decreased with increase in Ni-ion doping, even though the ionic conductivity was improved by the aliovalent B-site substitution. In addition, the presence of mixed valence states of Ni^{2+}/Ni^{3+} and Ti^{3+}/Ti^{4+} in a reducing atmosphere could affect the electrical conductivity in SYTN.

Fig. 3 shows the $Ti2p_{3/2}$ and $Ti2p_{1/2}$ spectra obtained using X-ray photoelectron spectroscopy (XPS). With increase in Ni-ion doping, the Ti2p peaks shifted to higher binding energy. When Ni^{2+} substitutes the Ti^{4+} in the lattice, a Ni-O-Ti structure is formed. Because of the greater electronegativity of Ni than Ti, the electrons are more localized around the Ni ions than Ti in this Ni-O-Ti structure. The reduced electron density at Ti results in an increase in the Ti2p binding energy. In addition, the Ti^{3+}/Ti^{4+} ratio is affected by the degree of Ni-ion doping, which can affect the oxygen vacancies, as shown by Eqs. (8) and (9).

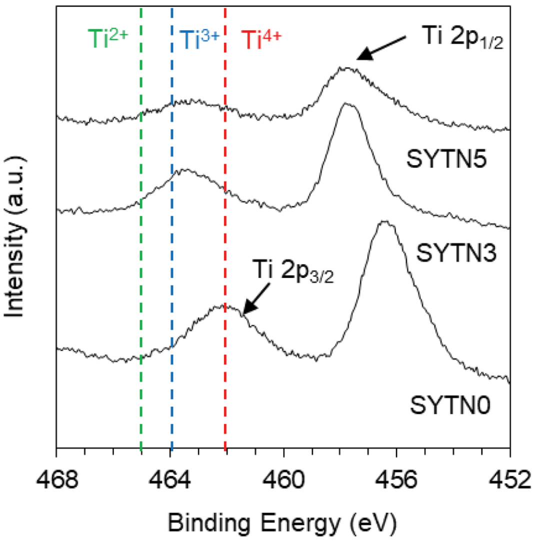

Fig. 3. $Ti2p_{3/2}$ and $Ti2p_{1/2}$ XPS spectra for SYTN0, SYTN3, and SYTN5.

$$O^{\times}_{O} \leftrightarrow V^{\cdot\cdot}_{O} + 2e' + \frac{1}{2}O_2 \tag{8}$$

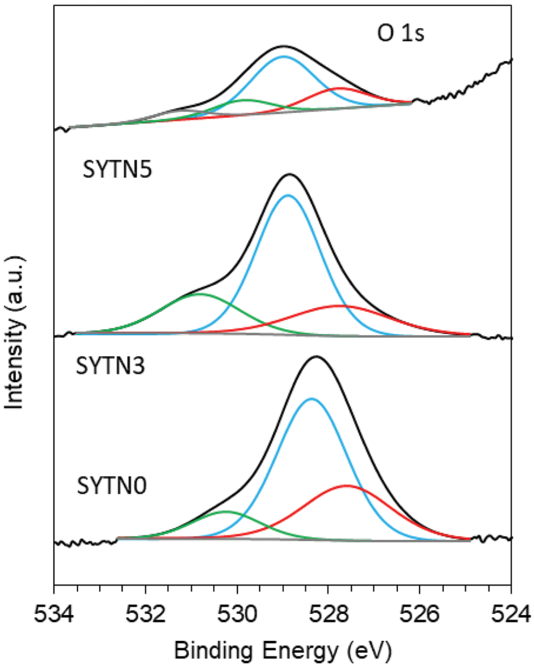

Fig. 4. O 1s XPS profiles and fitting for SYTN0, SYTN3, and SYTN5.

$$\mathrm{Ti}_{Ti}^{\times}+\mathrm{e}'\leftrightarrow \mathrm{Ti}_{Ti}' \qquad (9)$$

In addition, the oxygen vacancies may trap electrons, which would partially reduce Ti^{4+} to Ti^{3+}. Furthermore, the two electrons formed by the aliovalent substitution of Sr^{2+} by Y^{3+} (Eq. (6)) could increase the reduction of Ti (Eq. (9)), resulting in the formation of Ti^{3+}. In addition, different electronic states of surface oxygen species were identified in the O1s XPS profiles of SYTN0, SYTN3, and SYTN5, as shown in Fig. 4. With increase in Ni-ion doping, the O1s peaks shifted to higher binding energies. Three clear sub-peaks can be seen in the O1s XPS profiles of the SYTN0 and SYTN3 samples, and four sub-peaks were observed in that of the SYTN5 sample. The low-energy peak at 529 eV is associated with lattice oxygen in SYTN. The medium-energy peak at 530 eV is attributed to O^{2-} ions bonded to non-stoichiometric oxidized cations as a result of the presence of oxygen vacancies. The high-energy peak is attributed to the presence of loosely bound oxygen species on the surface, such as those in H_2O and OH groups. The atomic ratios of oxygen vacancies to lattice oxygen were calculated to be 0.18, 0.35, and 0.36 in SYTN0, SYTN3, and SYTN5, respectively. This result indicates that oxygen vacancies were formed as a result of oxygen loss around the Ti^{4+} ions, thus resulting in their reduction to Ti^{3+} via Eqs. (8)

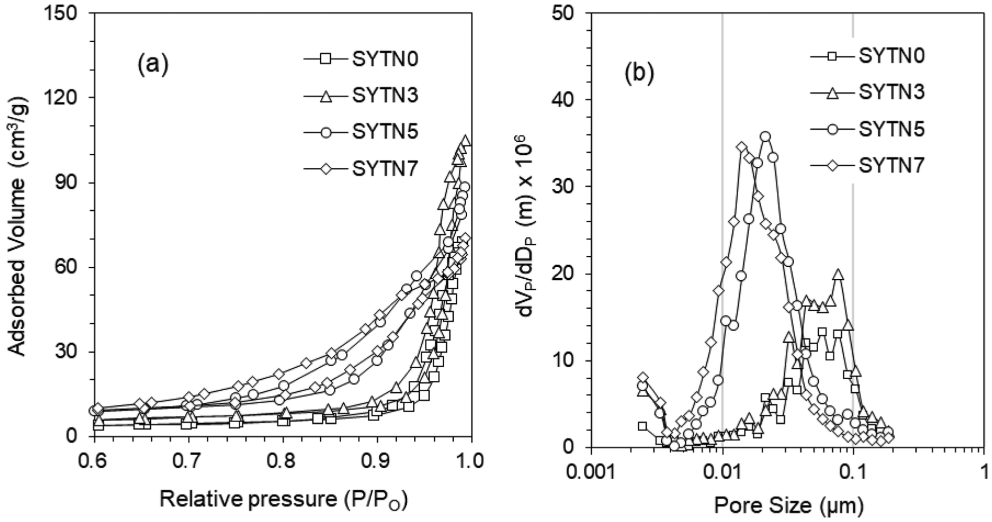

Fig. 5. (a) N_2 adsorption/desorption isotherms and (b) pore size distributions obtained using BET analysis of the synthesized mesoporous SYTN powder.

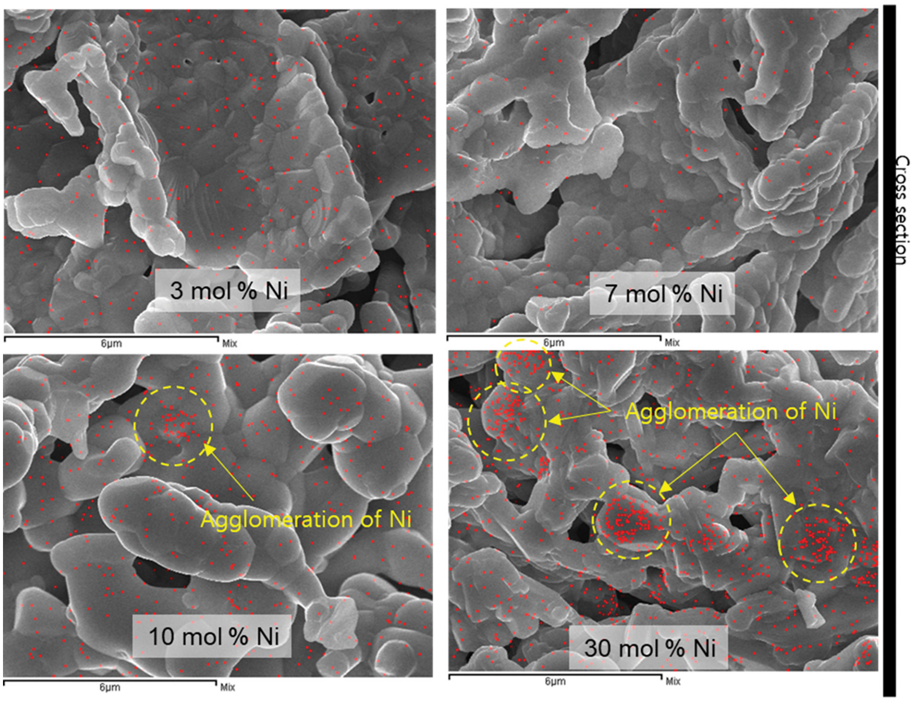

Fig. 6. SEM images of anode surfaces of SYTN3, SYTN5, SYTN10, and SYTN30.

Table 2. Surface areas and mean pore diameters obtained from BET analysis

	SYTN0	SYTN3	SYTN5	SYTN7
Surface area (m^2g^{-1})	8.73	12.84	19.42	20.10
Mean pore diameter (nm)	48.47	47.94	25.52	19.85

and (9), as well as via Ni-ion doping (Eq. (7)).

Fig. 5 shows the (a) N_2 adsorption/desorption isotherms and (b) pore size distribution of the synthesized mesoporous SYTN powder obtained using BET analysis. The N_2 adsorption/desorption analysis of the synthesized SYTN powder was performed to investigate the mesoporous structure. All samples showed sharp capillary condensation, indicating the formation of mesoporous structure. In addition, the BET surface area increased and the pore diameter decreased with increase in Ni-ion doping, as listed in Table 2. The BET surface areas were found to be 8.73, 12.84, 19.42, and 20.10 m^2g^{-1} in SYTN0, SYTN3, SYTN5, and SYTN7, respectively. Because of its relatively low melting temperature, Ni could act as a sintering aid during SYTN fabrication and sintering. Thus, the increase in Ni-ion doping would improve sample sintering, leading to an increase in the surface area and decrease in the pore diameter. Fig. 6 shows SEM images of the surfaces of the SYTN3,

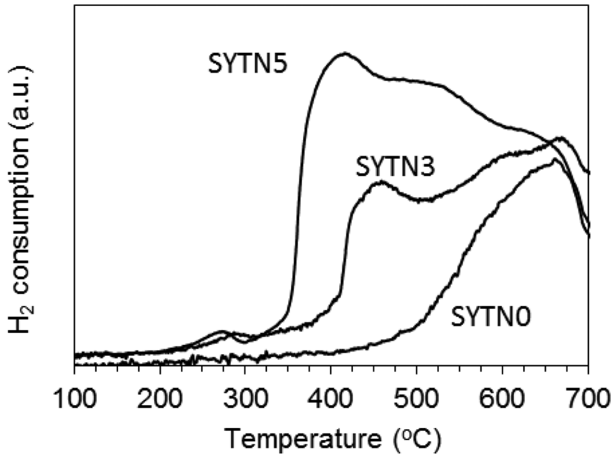

Fig. 7. H_2-TPR profiles of SYTN0, SYTN3, and SYTN5.

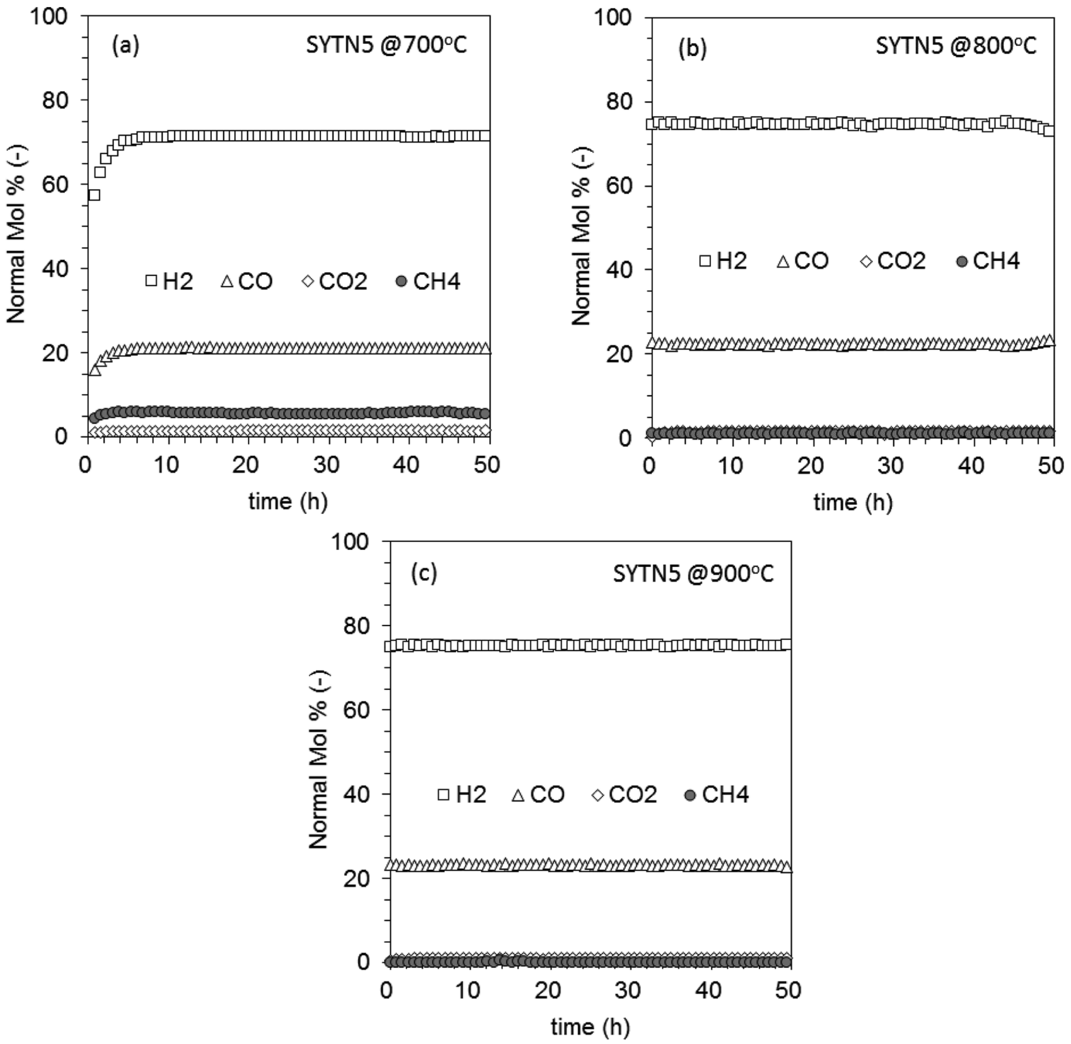

Fig. 8. Results of SMR reaction over the SYTN5 catalyst at 700, 800, and 900 °C.

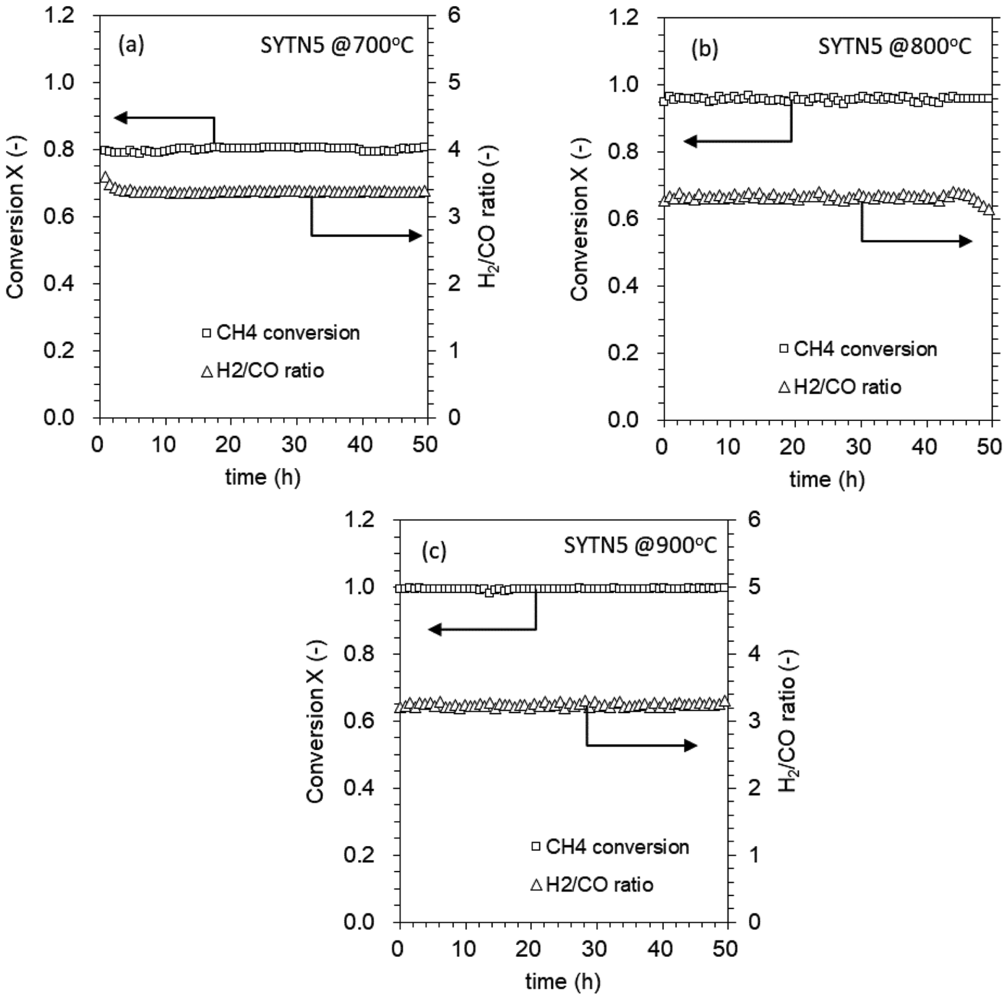

Fig. 9. CH_4 conversions and H_2/CO ratios of the SMR reaction over the SYTN5 catalyst at 700, 800, and 900 °C.

SYTN5, SYTN10 and SYTN30 samples. The Ni particles were uniformly dispersed in the SYTN3 and SYTN5 samples, but agglomerated nickel was observed in the SYTN10 and SYTN30 samples. This result indicates that, at high Ni-ion doping concentrations, Ni nanoparticles are exsolved to the surface and sintered at high temperatures under reducing conditions; this is consistent with previously reported observations [32,33]. Although the small amounts of Ni nanoparticles would be exsolved on the surface in the SYTN3 and SYTN5 samples, the agglomeration of Ni particles could be limited and might be difficult to detect in the SEM images. The H_2-TPR profiles of SYTN0, SYTN3, and SYTN5 are shown in Fig. 7. The location of the reduction peaks can be affected by the crystallite size, oxygen defects, binding strength, transition metal state or location, and degree of doping. With increase in Ni-ion doping, the reduction temperatures decreased because of the change in binding strength and the doping state, as well as the formation of oxygen defects.

As discussed, the very high catalytic activity of Ni-based anodes causes CH_4 pyrolysis, resulting in carbon deposition, which decreases the electrochemical performance and increases the mass transfer resistance. Typically, oxide-based materials exhibit very low activity for catalytic CH_4 oxidation, making them unsuitable anode materials despite their immunity to carbon deposition. However, the oxygen vacancies formed by Ni^{2+} substitution (Eq. (7)) could improve the CH_4 oxidation activity. Figs. 8 and 9 show the results obtained for the SMR reaction for syngas (H_2+CO) production (Eqs. (1) and (2)) over the SYTN5 catalyst at 700, 800, and 900 °C. The molar ratio of CH_4 and H_2O was 1 : 1, the GHSV was 6,000 h^{-1}, and the SYTN5 catalyst quantity was 0.4 g. The CH_4 conversions were 0.80, 0.96, and 0.99 at 700, 800, and 900 °C, respectively, and the H_2 to CO (H_2/CO) ratios were 3.38, 3.32, and 3.24 at 700, 800, and 900 °C, respectively, which are close to the theoretical values (between 3 and 4) according to Eqs. (1) and (2).

Fig. 10 shows the impedance spectra obtained for SYTN0 and SYTN5 in button-type anode symmetric cells at 900 °C under H_2 or CH_4 fuel conditions. In addition, impedance spectra of symmetric cells containing the Ni/YSZ anode are shown for comparison. The ohmic resistance was excluded to allow the analysis of the effects of the anode polarization resistance. Under H_2 fuel conditions, the polarization resistances of the anode side in the half cells were 0.90, 0.77, and 0.40 Ω cm^2 for the SYTN0, SYTN5, and Ni/YSZ anodes, respectively. Under CH_4 fuel conditions, the polarization resistance of the anode side in the half cells increased to 6.69, 4.00, and 9.77 Ω cm^2 for the SYTN0, SYTN5, and Ni/YSZ

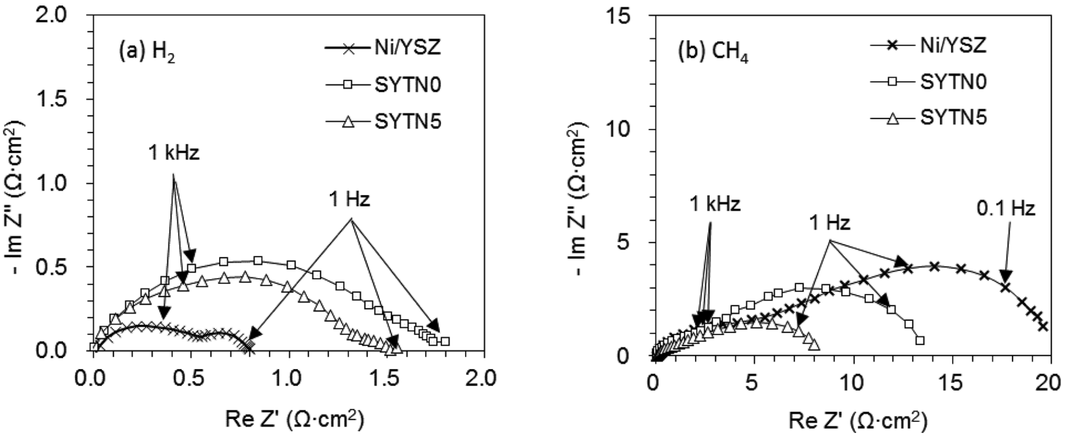

Fig. 10. Impedance spectra of Ni/YSZ, SYTN0, and SYTN5 in button-type anode symmetric cells at 900 °C under H_2 and CH_4 fuel conditions.

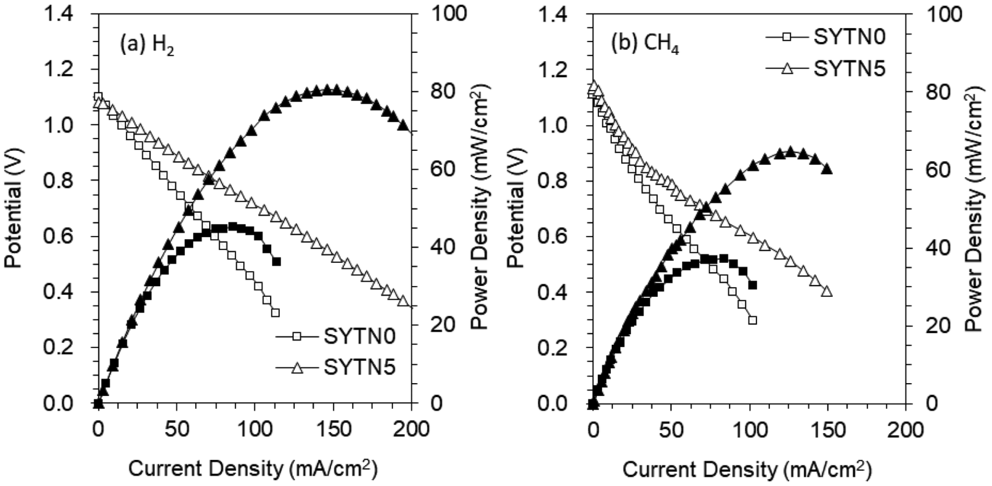

Fig. 11. I-V characteristics of the SYTN0 and SYTN5 anode cells at 900 °C under H_2 and CH_4 fuel conditions.

anodes, respectively. Although the interpretation of the impedance spectra of multilayered fuel cells is very complicated and often ambiguous, previous studies allow us to make a tentative analysis. We identified arc frequencies at 1 kHz and 1 Hz. The high-frequency arcs (1 kHz) can be attributed to oxygen-ion diffusion between the electrolyte and the triple-phase boundary (TPB) sites in the anode. The low-frequency arcs (less than 1 Hz) can be attributed to slow reactions such as mass transfer related to the gas-phase diffusion resistance. Under H_2 fuel conditions, the radius of the high-frequency arc in the spectrum of the Ni/YSZ anode is much smaller than that in the spectra of the SYTN0 and SYTN5 anodes because of the excellent ionic conductivity of YSZ. In addition, the ionic conductivity or MIEC properties exhibited by the SYTN5 anode resulted in a decrease in the radius of the high-frequency arc in the impedance spectra. Under CH_4 fuel conditions, the radii of the low-frequency arcs increased compared to those obtained under H_2 conditions in the spectra of all anodes because of slow gas-phase diffusion and slow CH_4 oxidation. In particular, the radius of the low-frequency arc in the spectrum of the Ni/YSZ anode increased significantly, likely because carbon deposition occurred. As mentioned, the high catalytic activity of the Ni/YSZ anode is a significant cause of carbon deposition.

Fig. 11 shows the current-voltage (I-V) characteristics of SYTN0 and SYTN5 anode cells at 900 °C in the presence of humidified H_2 or humidified CH_4. The YSZ electrolyte-supported cells containing LSM/YSZ/SYTN were prepared to allow us to compare the effect of Ni-ion doping in the SYT anode. The results were acquired after stabilizing the system for 2 h. The maximum power density obtained under H_2 fuel conditions was 45.3 and 80.6 mWcm^{-2} for the SYTN0 and SYTN5 anodes, respectively. Under CH_4 fuel conditions, the maximum power density decreased to 37.3 (85.7%) and 64.7 (80.3%) mW·cm^{-2} in the SYTN0 and SYTN5 anodes, respectively. The excellent electrochemical properties exhibited by the SYTN5 anode resulted in improved cell performance. In addition, the oxygen vacancies induced by the doping of Ni^{2+} at the Ti^{4+} sites in the SYTN5 anode improved the cell performance. Under CH_4 fuel conditions, the open circuit voltages (OCVs) at 900 °C were 1.11 and 1.14 V for SYTN0 and SYTN5, respectively, which are slightly higher than the theoretical values (1.05-1.08 V) for H_2 oxidation and lower than the theoretical values (1.2-1.3 V) for CH_4 oxidation in the YSZ electrolyte at 900 °C. Therefore, the electrochemical oxidation of H_2 produced via the SMR is likely the major contribution to the OCV in the SYTN5 anode cell, although the electrochemical oxidation of CH_4 could also contribute to the OCV. The decrease in the performance of the cell containing the SYTN0 anode was small relative to that containing the SYTN5 anode, but the poor inherent catalytic activity of the SYTN0 anode for CH_4 oxidation would minimize carbon deposition.

CONCLUSION

$Sr_{0.92}Y_{0.08}Ti_{1-x}Ni_xO_{3-\delta}$ (SYTN) having a perovskite structure was investigated as a direct internal steam methane reforming catalyst for solid oxide fuel cell anodes. To analyze the effect of Ni-ion doping, 0, 3, and 5 mol% Ni was doped at the B-sites in $Sr_{0.92}Y_{0.08}TiO_{3-\delta}$ (SYT). Each Ni^{2+} cation substitutes Ti^{4+} in SYT to form an oxygen vacancy with two electron holes, which act as oxygen-ion conductors. The electrical conductivity of SYTN decreased with increase in Ni-ion doping. At 900 °C, the electrical conductivity was 0.95, 0.24, and 0.06 $S\cdot cm^{-1}$ for the SYTN0, SYTN3, and STYN5 anodes, respectively, and the MIEC property exhibited by the SYTN anode could be a possible explanation for the decrease in the electrical conductivity with increase in Ni-ion doping. The CH_4 conversion for the steam methane reforming reaction using the STYN5 anode was 0.80, 0.96, and 0.99 at 700, 800, and 900 °C, respectively, and the H_2-to-CO ratio was 3.38, 3.32 and 3.24 at 700, 800, and 900 °C, respectively, which are close to the theoretical values for the steam methane reforming and water-gas shift reactions. In addition, the introduction of ionic conductivity or MIEC properties to the SYTN5 anode material reduced the anode polarization resistance under H_2 and CH_4 fuel conditions. The maximum power densities under H_2 fuel conditions were 45.3 and 80.6 $mW\cdot cm^{-2}$ for the SYTN0 and SYTN5 anodes, respectively. Under CH_4 fuel conditions, the maximum power densities decreased to 37.3 (85.7%) and 64.7 (80.3%) mW cm^{-2} for the SYTN0 and SYTN5 anodes, respectively. Furthermore, the electrochemical oxidation of H_2 produced via the SMR is the major contributor to the OCV in the SYTN5 anode cell, although the electrochemical oxidation of CH_4 could also contribute to the OCV. The excellent electrochemical properties of the SYTN5 anode improved the cell performance. In addition, the oxygen vacancies induced by Ni-ion doping at the Ti^{4+} sites in the SYTN5 anode improved the cell performance.

ACKNOWLEDGEMENTS

This work was supported by the Innovation Lab support program for material, parts, equipment (20012555, Commercialization of nanocarbon composites materials in electric and electronic display and energy industries) funded by the Ministry of Trade, industry & Energy (MOTIE, Korea).

REFERENCES

1. Z. Lyu, W. Shi and M. Han, *Appl. Energy*, **228**, 556 (2018).
2. Fuel Cell Handbook 7th Edition, U.S. Department of Energy, EG&G Technical Services Inc., West Virginia (2004).
3. J. M. Klein, M. Hénault, C. Roux, Y. Bultel and S. Georges, *J. Power Sources*, **193**, 331 (2009).
4. L. Barelli, G. Bidini, A. Di Michele, L. Gammaitoni, M. Mattarelli, F. Mondi and E. Sisani, *Int. J. Hydrogen Energy*, **44**, 16582 (2019).
5. H. Su and Y. H. Hu, *Chem. Eng. J.*, **402**, 126235 (2020).
6. A. D. Giuliano and K. Gallucci, *Chem. Eng. Process*, **130**, 240 (2018).
7. L. Fan, L. Van Biert, A. T. Thattai, A. H. M. Verkooijen and P. V. Aravind, *Int. J. Hydrogen Energy*, **40**, 5150 (2015).
8. Y. Matsuzaki and I. Yasuda, *J. Electrochem. Soc.*, **147**, 1630 (2000).
9. Q. Zhao, Y. Wang, Y. Wang, L. Li, W. Zeng, G. Li and C. Hu, *Int. J. Hydrogen Energy*, **45**, 14281 (2020).
10. A. J. Jacobson, *Chem. Mater.*, **22**, 660 (2010).
11. J. W. Fergus, R. Hui, X. Li, D. P. Wilkinson and J. Zhang, *Solid oxide fuel cells: Materials properties and performance*, CRC press, Boca Raton (2019).
12. A. Atkinson, S. Barentt, R. J. Gorte, J. T. S. Irvine, A. J. Mcevoy, M. Mogensen, S. C. Singhal and J. Vohs, *Nat. Mater.*, **3**, 17 (2004).
13. J. Hanna, W. Y. Lee, Y. Shi and A. F. Ghoniem, *Prog. Energ. Combust.*, **40**, 74 (2014).
14. S. I. Lee, J. M. Vohs and R. J. Gorte, *J. Electrochem. Soc.*, **151**, A1319 (2004).
15. H. Kim, C. Lu, W. L. Worrell, J. M. Vohs and R. J. Gorte, *J. Electrochem. Soc.*, **149**, A247 (2002).
16. M. Suzuki, H. Sasaki, S. Otoshi, A. Kajimura and M. Ippommatsu, *Solid State Ionics*, **62**, 125 (1993).
17. N. Mahato, A. Banerjee, A. Gupta, S. Omar and K. Balani, *Prog. Mater. Sci.*, **72**, 141 (2015).
18. R. J. Gorte, S. Park, J. M. Vohs and C. Wang, *Adv. Mater.*, **12**, 1465 (2000).
19. H. Ding, D. Zhou, S. Liu, W. Wu, Y. Yang, Y. Yang and Z. Tao, *Appl. Energy*, **233-234**, 37 (2019).
20. Z. Bian, Z. Wang, B. Jiang, P. Hongmanorom, W. Zhong and S. Kawi, *Renew. Sustain. Energy Rev.*, **134**, 110291 (2020).
21. K. Kim, C. Lim and J. W. Han, *Korean J. Chem. Eng.*, **37**, 1295 (2020).
22. H. Jeong, D. Kim, B. Sharma, J. H. Noh, K. T. Lee and J. H. Myung, *Korean J. Chem. Eng.*, **37**, 1440 (2020).
23. J. B. Goodenough and Y. H. Huang, *J. Power Sources*, **173**, 1 (2007).
24. L. Shu, J. Sunarso, S. S. Hashim, J. Mao, W. Zhou and F. Liang, *Int. J. Hydrogen Energy*, **44**, 31275 (2019).
25. J. Cao, C. Su, Y. Ji, G. Yang and Z. Shao, *J. Energy Chem.*, **57**, 406 (2021).
26. M. A. Gwan and J. W. Yun, *J. Electroceram.*, **40**, 171 (2018).
27. J. H. Kim and J. W. Yun, *J. Electrochem. Sci. Te.*, **10**, 335 (2019).
28. J. M. Lee and J. W. Yun, *Ceram. Int.*, **42**, 8698 (2016).
29. J. H. Kim and J. W. Yun, *J. Electrochem. Sci. Te.*, **9**, 133 (2018).
30. E. K. Park, S. Lee and J. W. Yun, *Appl. Surf. Sci.*, **429**, 171 (2018).
31. H. S. Kim, Y. Jeon, J. H. Kim, G. Y. Jang, S. P. Yoon and J. W. Yun, *Appl. Surf. Sci.*, **510**, 145450 (2020).
32. D. Papargyriou and J. T. S. Irvine, *Solid State Ionics*, **288**, 120 (2016).
33. Y. Gao, D. Chen, M. Saccoccio, Z. Lu and F. Ciucci, *Nano Energy*, **27**, 499 (2016).